On the mass of dense star clusters in starburst galaxies from spectrophotometry

J.-J. Fleck,[1][★] C. M. Boily,[1] A. Lançon[1] and S. Deiters[2]

[1]*Observatoire astronomique, 11 rue de l'Université, F-67000 Strasbourg, France*
[2]*School of Mathematics, University of Edinburgh, King's Buildings, Edinburgh EH9 3JZ*

ABSTRACT

The mass of unresolved young star clusters derived from spectrophotometric data may well be off by a factor of 2 or more once the migration of massive stars driven by mass segregation is accounted for. We quantify this effect for a large set of cluster parameters, including variations in the stellar initial mass function (IMF), the intrinsic cluster mass, and mean mass density. Gas-dynamical models coupled with the Cambridge stellar evolution tracks allow us to derive a scheme to recover the *real* cluster mass given measured half-light radius, one-dimensional velocity dispersion and age. We monitor the evolution with time of the ratio of real to apparent mass through the parameter η. When we compute η for rich star clusters, we find non-monotonic evolution in time when the IMF stretches beyond a critical cut-off mass of $25.5\,\mathrm{M_\odot}$. We also monitor the rise of colour gradients between the inner and outer volume of clusters: we find trends in time of the stellar IMF power indices overlapping well with those derived for the Large Magellanic Cloud cluster NGC 1818 at an age of 30 Myr. We argue that the core region of massive Antennae clusters should have suffered from much segregation despite their low ages. We apply these results to a cluster mass function, and find that the peak of the mass distribution would appear to observers shifted to *lower* masses by as much as 0.2 dex. The star formation rate derived for the cluster population is then underestimated by from 20 to 50 per cent.

Key words: methods: numerical – stars: evolution – stars: kinematics – stars: luminosity function, mass function – galaxies: clusters: individual: NGC 1818 – galaxies: star clusters.

1 INTRODUCTION

Star clusters are traditionally thought of as old primordial structures with ages ranging up to a Hubble time, hence the emphasis of theoretical modelling on their long-term evolution (e.g. Spitzer 1987; see Meylan & Heggie 1997 for a review). However, the wealth of massive young clusters with spectroscopic ages of less than 100 Myr observed with the *Hubble Space Telescope* in interacting galaxies (e.g. the Antennae, M81/82) has driven much interest in recent years to the understanding of their formation and early evolution. Closer to us, the Large Magellanic Cloud (LMC) hosts a set of young clusters (Elson, Freeman & Lauer 1989; Elson 1991), of which some show signs of primordial mass segregation. The cluster NGC 1818 is one such cluster where colour gradients are difficult to account for other than as a result of their formation history (Hunter et al. 1997). These issues clearly have bearing on the subsequent dynamical

evolution and photometric properties of clusters and their immediate surroundings (e.g. Lamers, Anders & de Grijs 2006).

To understand very young clusters in quantitative detail poses a particular challenge to theorists since realistic models must account both for the dynamics and the rapidly evolving photometric properties of a young stellar population. In this contribution, we aim to identify evolutionary trends that lead potentially to large errors when measuring the mass of an unresolved cluster with photometry and spectroscopy, an effect that bears on all observable cluster properties.

When in dynamical equilibrium, the virial theorem gives an exact relation between mass M and mean three-dimensional velocity dispersion σ:

$$M = \frac{|W|}{\sigma^2} \equiv \frac{r_g \sigma^2}{G}, \tag{1}$$

where W is the gravitational potential energy, G the gravitational constant and r_g a radius so defined. All quantities entering equation (1) must be matched with observables in projection. The line-of-sight velocity dispersion σ_{los}^2 equals $\sigma^2/3$ for an isotropic

[★]E-mail: jfleck@astro.u-strasbg.fr

velocity field, while the gravitational radius may be expressed in terms of the projected half-light radius R_{hl}[1] as

$$r_g \approx \frac{5}{2} \times \frac{4}{3} R_{hl}, \tag{2}$$

where the numerical factor of 5/2 gives a rough conversion to a wide-range of clusters fitted with a King mass profile, and the factor of 4/3 comes from projection on the sky (e.g. Spitzer 1987; McCrady, Gilbert & Graham 2003; section 1.2). Equation (2) applies when light traces mass throughout the cluster. With this in mind we may isolate for M in equation (1) to obtain

$$M = \eta \frac{R_{hl} \sigma_{los}^2}{G}, \tag{3}$$

where the dimensionless parameter $\eta \simeq 10$. Several authors have used $\eta \approx 10$ combined with spectrophotometric data to derive M from equation (3). Such mass estimates can be compared to masses derived from synthetic stellar populations of the same King models fitted to the data to set constraints on the stellar initial mass function (IMF). For instance, the stellar population of massive Antennae clusters appears to be inconsistent with a universal (field) stellar IMF (Smith & Gallagher 2001; Mengel et al. 2002). And several clusters in the galaxy M82 are found to be overluminous with respect to their mass, suggesting a top-heavy stellar IMF in these clusters (Smith & Gallagher 2001; McCrady et al. 2003).

The above studies have taken a fixed value of η for clusters of ages up to $t = 100$ Myr. This simplification, while intuitively appealing, was shown recently not to be of universal use for massive clusters (Boily et al. 2005). Dense, populous clusters will fill the entire range of stellar masses drawn from the IMF. This has the effect of dramatically reducing the mass-segregation time-scale compared with the relaxation time-scale and driving heavy (bright) stars to the centre of the cluster. The measurements of R_{hl} and σ_{los} are then biased to values associated with a specific stellar population, and not the cluster as a whole as assumed in deriving equation (3). When the density of the cluster is low (at a given number of stars), this bias is reduced and η remains constant over time to a good approximation. Using theoretical gas-dynamical models, Boily et al. (2005) found a rough threshold of mean surface density such that when the initial cluster density is $\langle \Sigma \rangle \approx 10^4 \, M_\odot \, pc^{-2}$ or more, masses derived assuming constant η systematically underestimate the real mass by a factor of a few.

This contribution explores a fuller range of parameters and addresses other issues (colour gradients, systematics) not covered by Boily et al. (2005). In the next section, we briefly recall the dynamical time-scales relevant to the problem and show explicitly why a bias should be anticipated when deriving the mass of rich, dense clusters. In Section 3, we give details of the numerical approach used to conduct the study. In Section 4, we discuss how the models were analysed and quantify numerical and systematic errors. Section 5 presents the results of our survey. In Section 6, we apply these results to the profiling of the stellar mass function and colour gradients in clusters. We also explore their implication for a cluster mass function, and show that the star formation rate (SFR) inferred from cluster populations may be strongly biased to lower values. The concluding section introduces a diagram that relates observed cluster properties to their underlying potential and draws attention to future developments.

---

[1] By convention and when possible, projected quantities are denoted with upper case letters.

2 THE DYNAMICS OF MASS SEGREGATION

Two conditions have to be met for equation (3) to be applicable. First, all stellar components should be in dynamical equilibrium, a sensible assumption whenever the cluster age exceeds the virialization time-scale, i.e. several system crossing time t_{cr}, where

$$t_{cr} \equiv \frac{2 \, r_{hm}}{\sigma} \tag{4}$$

with r_{hm} being the spherical half-mass radius. The mechanics of virialization leads to equilibrium velocity distribution functions independent of stellar masses when all stars have the same radial distribution. Collisional gravitational dynamics, on the other hand, sets a trend towards equipartition of kinetic energy between stars of different masses as the system evolves. The resulting instability has been studied by Spitzer (1969); see also Khalisi, Amaro-Seoane & Spurzem (2006) for a recent work. For two-component systems of individual masses m_1 and m_2, this situation is expressed as

$$\frac{1}{2} \, m_1 \, \sigma_1^2 = \frac{1}{2} \, m_2 \, \sigma_2^2, \tag{5}$$

and hence the ratio of squared velocities of the stars equals the inverse ratio of their masses: heavier stars have lower velocities on the mean, and drop to the centre of the cluster. The state of dynamical equilibrium is a good approximation to the dynamics only when the migration of the heavy stars takes place over long time-scales.

Secondly, the light should trace the mass so that half-light and half-mass radii are identical. When this is not the case, the mass M may be derived from either of the two relations

$$M = \eta_0 \frac{R_{hm} \sigma_{m1d}^2}{G} \quad \text{and} \quad M = \eta \frac{R_{hl} \sigma_{los}^2}{G}, \tag{6}$$

where σ_{m1d} is the mass-weighted velocity dispersion in projection along the line of sight, and σ_{los} its light-weighted analogue, i.e. the line-of-sight velocity dispersion most directly accessible to observation. $\eta_0 \approx 10$ is the reference value mentioned already. These relations combine to give

$$\eta = \eta_0 \frac{R_{hm} \sigma_{m1d}^2}{R_{hl} \sigma_{los}^2} \tag{7}$$

and hence $\eta \neq \eta_0$ whenever light and mass follow different runs with R. Since bright stars carry all the light but a small fraction of the total mass, we expect $\eta > \eta_0$ as the massive stars migrate to the centre, and both R_{hm} and σ_{m1d}, weighted through the near-static total mass distribution, remain essentially constant.

2.1 Characteristic time-scales

The total mass distribution of a star cluster evolves slowly over the relaxation time t_r of single-population clusters given by

$$\frac{t_r}{t_{cr}} \simeq \frac{0.138}{2} \left(\frac{r_{hm}}{r_g} \right)^{1/2} \frac{N}{\ln(0.4 \, N)}, \tag{8}$$

which is identical to Meylan & Heggie (1997, section 7) once equation (4) is taken into account where we used $2r_{hm}$ in the definition rather than r_g. N is the number of member stars and the ratio $r_{hm}/r_g \approx 0.4$ for a wide range of model fits to observed clusters.

With $N = 500\,000$, $r_{hm} = 4/3 \, R_{hm} = 1.3$ pc (suggested from massive clusters data) and $\sigma = \sqrt{3} \sigma_{los} = 26 \, km \, s^{-1}$, we find a relaxation time

$$t_r \approx 1800 \, t_{cr} \approx 180 \, \text{Myr} \tag{9}$$

and hence no massive cluster with an age of less than 100 Myr would be expected to show signs of evolution due to two-body relaxation. It is this argument that led to the widely used assumption of no evolution of clusters in young starburst galaxies. However, Farouki & Salpeter (1982) pointed out that the trend towards equipartition is accelerated as the mass spectrum $\{m_j\}$ of stars is widened; their analysis suggests that the mass segregation will take place on a time-scale t_{ms} given by (Spitzer 1987)

$$\frac{t_{ms}}{t_r} \simeq \frac{\pi}{3} \frac{\langle m \rangle}{m_{max}} \frac{\overline{\rho}}{\rho} \left(\frac{r_{hm}}{r_g} \right)^{3/2}, \tag{10}$$

where $\overline{\rho} \equiv (M/2)/(4\pi r_{hm}^3/3)$ is the mean density inside the three-dimensional half-mass radius (an overline denotes averaging over space, and brackets averaging by mass); and $m_{max} = \max\{m_j\}$, $j = 1, \dots, J$. Note that $t_{ms} \approx t_r$ when the mass spectrum is narrow, i.e. we recover the single-component cluster relaxation time. The mean mass $\langle m \rangle \approx 0.7\,M_\odot$ for a standard Kroupa IMF (Kroupa 2002). Going back to the numerical example given in the above, setting $m_{max} = 20\,M_\odot$ in equation (10) already reduces the mass segregation time-scale t_{ms} to a few Myr, suggesting that mass segregation will be effective over the life of massive stars.

2.2 Example: two-mass component systems

Consider a cluster with two stellar masses, $m_1 < m_2$, mean surface density Σ and mass weighted squared velocity dispersion $\langle \sigma^2 \rangle$. Each component i has a velocity dispersion σ_i, a surface density Σ_i and a surface brightness Λ_i. The equilibrium velocity dispersion assuming equation (5) leads to

$$\langle \sigma^2 \rangle = \sigma_1^2 \frac{\Sigma_1}{\Sigma} \left(1 + \frac{\Sigma_2}{\Sigma_1} \frac{\sigma_2^2}{\sigma_1^2} \right)$$
$$= \sigma_1^2 \frac{\Sigma_1}{\Sigma} \left(1 + \frac{\Sigma_2}{\Sigma_1} \frac{m_1}{m_2} \right). \tag{11}$$

On the other hand, using light to weigh the quantities yields

$$\sigma_{lw}^2 = \sigma_1^2 \frac{\Lambda_1}{\Lambda} \left(1 + \frac{\Lambda_2}{\Lambda_1} \frac{m_1}{m_2} \right). \tag{12}$$

Since the stellar IMF is peaked at the low-mass end and $m_1 < m_2$, the surface density of the second component $\Sigma_2 < \Sigma_1 \approx \Sigma$. The same quantities weighted by light yield a different result. Since $m_1 < m_2$, the brightness $\Lambda_1 \ll \Lambda_2 \approx \Lambda$, so that generally $\Lambda_2 m_1 > \Lambda_1 m_2$ for a standard IMF (see Section 4.1.1). This gives the following, approximate, relations

$$\langle \sigma^2 \rangle \approx \sigma_1^2 \quad \text{and} \quad \sigma_{lw}^2 \approx \sigma_2^2. \tag{13}$$

By the same line of arguments, we obtain for the radii

$$R_{hm} \approx R_{hm1} \quad \text{and} \quad R_{hl} \approx R_{hm2}. \tag{14}$$

Owing to mass segregation, we anticipate $\sigma_1^2 > \sigma_2^2$ and $R_{hm1} > R_{hm2}$. As a result, η computed from equation (7) gives

$$\eta = \eta_0 \frac{R_{hm1} \sigma_1^2}{R_{hm2} \sigma_2^2} > \eta_0. \tag{15}$$

This reasoning will hold true for multimass cases in general since we may replace m_1 by $\langle m \rangle$ and m_2 by m_{max}: light-weighted quantities trace positions and velocities of the heavier stars, whereas the global potential and kinematics are set by the less-massive stars.

3 NUMERICAL METHOD

3.1 Gas models

Large stellar systems share several thermodynamical properties with classical gases (Lynden-Bell & Wood 1968). A cluster composed of stars of different masses may be likened to a set of concentric spheres of ideal gas satisfying Poisson's equation. Larson (1970) pioneered a method based on moments of the Boltzmann equation by which energy ('heat') flows through the system as it would in a fluid. The temperature of a stellar system, then, is identified with the local square velocity dispersion so that heat may be transported from low dispersion regions to high-dispersion regions (owing to the negative heat capacity of gravity). Stellar collisions are treated through a local heat conduction equation (Lynden-Bell & Eggleton 1980) which may be calibrated to give evolutionary tracks virtually indistinguishable from those obtained from N-body calculations (see Spurzem & Takahashi 1995).

Bettwieser & Inagaki (1985) give a good insight of the hydrodynamical spirit of the model but note that their closure equation requires modification for agreement with Fokker–Planck models (Spurzem & Takahashi 1995). A complete and anisotropic formulation based on moments of the Boltzmann equation can be found in Louis & Spurzem (1991).

3.2 Integration code

The numerical code SPEDI[2] that we use is based largely on the formulation for anisotropic stellar systems due to Louis & Spurzem (1991). It was developed further by Spurzem & Takahashi (1995). The equations are set on a logarithmic mesh using a scheme which is forward-differencing in space and centred in time. Time integration was performed iteratively using a semi-implicit Newton–Raphson–Henyey method. The gravitational potential is evaluated from the updated (total) density profile directly from Poisson's equation.

SPEDI has been adapted by one of us (Deiters 2001) to include a model of stellar evolution. We refer to the resulting code as GASTEL. Stars are evolved according to the Cambridge stellar evolution tracks, which are available in a convenient analytical form (Pols et al. 1998; Hurley, Pols & Tout 2000). By the end of their lives, stars have lost a significant fraction of their mass. This mass lost by stars is expelled instantaneously from the cluster. However, we may still compute η in the approximation that the total cluster mass remains constant for short evolution times since in reality the gas will not leave the cluster instantly (see Section 6.3).

All variables are evaluated on a 200-point grid in the N-body units given by Heggie & Mathieu (1986). The constant logarithmic width between two grid points is $d \ln r \approx 0.095$. Spatial resolution in the centre is excellent (152 mesh points to the initial half-mass radius at 0.6 numerical units) and the grid extends up to 60 numerical units.

3.3 Calibration, tests

The only free parameter in the equations of the gaseous model is the value of the conductivity (sometimes denoted λ). It is then adjusted to be consistent with N-body calculations and to recover the core collapse time in the case of a system of N identical masses (Bettwieser & Inagaki 1985; Section 2.2; see also Spurzem 1992). Several tests have been conducted to compare gas cluster models with Fokker–Planck integrations and direct N-body calculations (Giersz &

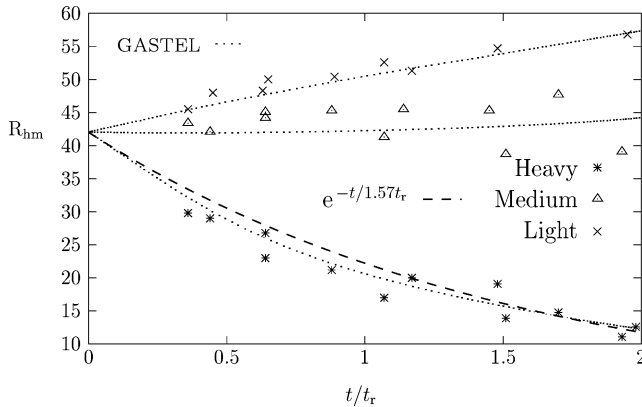[2] Further details at http://www.ari.uni-heidelberg.de/gaseous-model/.

Figure 1. Run of half-mass radius for a three-component Plummer model versus time. The three stellar masses 2/5, 1 and 5/2 were drawn from a Salpeter IMF. The symbols are for data points lifted from fig. 1 of Spitzer & Shull (1975). The dash is an exponential decay $\propto \exp(-t/1.57t_r)$.

Heggie 1994; Giersz & Spurzem 1994; Spurzem & Takahashi 1995). Most of these tests were for two-component models of modest mass ratios, while the stellar mass range of interest here covers nearly two decades. We therefore checked explicitly that the numerical set-up correctly reproduces the dynamics of multimass models with a broad mass spectrum. Spitzer & Shull (1975) presented results of mass segregation from Fokker–Planck calculations of three-component Plummer models. The three masses were in the ratio 2/5:1:5/2 and drawn from a Salpeter IMF. Fig. 1 graphs the time evolution of the half-mass radius of each component as obtained with GASTEL (dotted curves) along with the results read off fig. 1 of Spitzer & Shull (1975). We find very good agreement with their data. In particular, we find the evolution for the most massive stars well recovered from an exponential decay of the form $R_{\mathrm{hm}}(t) = R_{\mathrm{hm}}(0) \exp(-t/1.57t_r)$.

4 METHOD OF ANALYSIS AND ERROR ESTIMATES

GASTEL computes for each dynamical mass group the mass distribution and velocity dispersion on a radial grid. The mass density $\rho(r)$ and velocity dispersion $\sigma(r)$ of each group are integrated along the line of sight to obtain the projected distributions at cylindrical radius R using the relation $r^2 = R^2 + z^2$:

$$\Sigma(R) = \int_{-\infty}^{+\infty} \rho(r)\,\mathrm{d}z, \qquad (16)$$

$$\Sigma\,\sigma_{\mathrm{los}}^2(R) = \int_{-\infty}^{+\infty} \rho(r)\,\sigma^2(r)\,\mathrm{d}z. \qquad (17)$$

The half-mass radius and mean velocity dispersion are computed for each mass group. System averages are then computed by summing over all groups using either the density or the light flux as statistical weight. A stand-alone programme is used to pick the most luminous stellar mass at each output time. This approach allows us to combine the properties of different stars as desired in the analysis, without having to rerun the simulation with a different set-up. For example, it will prove illuminating in the first instance to monitor physical quantities attached to the most luminous stars alone as function of time, before profiling the system including contributions from all the stars (see Section 4.3).

4.1 Mass sampling

Our overall goal is to describe accurately the early evolution of a cluster. This suggests that we seek out a relation between the spectrum of stellar masses and the time-scale for dynamical evolution given by equation (10), before selecting a set of stellar mass groups.

4.1.1 Stellar IMF

The field stellar IMF in the solar neighbourhood sets a standard reference (Kroupa 2002). This distribution function of single stars of mass m is well fitted by a piece-wise power law,

$$f(m) \propto \begin{cases} m^{-\alpha} & \text{if } m < 1\,\mathrm{M}_\odot, \\ m^{-\beta} & \text{if } 1\,\mathrm{M}_\odot < m < 10\,\mathrm{M}_\odot, \\ m^{-\gamma} & \text{if } m > 10\,\mathrm{M}_\odot, \end{cases} \qquad (18)$$

where $\alpha = 1.30$, $\beta = 2.35$, and $\gamma = 4.0$. The value of α has significant uncertainties ± 0.7 (Kroupa 2002) whose implications will be discussed in Section 5.4. Stellar demographics are computed by integrating $f(m)\,\mathrm{d}m$ up from a lower value which we set above the brown dwarf limit at $0.10\,\mathrm{M}_\odot$. If the real mass distribution extended to $0\,\mathrm{M}_\odot$ with the same power law, our cut at $0.1\,\mathrm{M}_\odot$ would allow us to account for 80 per cent of the actual mass and 99.9 per cent of the actual emitted light of the low-mass stars ($M < 1\,\mathrm{M}_\odot$). The mean stellar mass computed from equation (18) is

$$\langle m \rangle = \frac{\int_{0.1\,\mathrm{M}_\odot}^{\infty} m\,f(m)\,\mathrm{d}m}{\int_{0.1\,\mathrm{M}_\odot}^{\infty} f(m)\,\mathrm{d}m} \approx 0.7\,\mathrm{M}_\odot. \qquad (19)$$

However, note that due to discrete and non-uniform sampling, in most of the simulations we have $\langle m \rangle \approx 0.85\,\mathrm{M}_\odot$.

4.1.2 The mass spectrum and the importance of stellar evolution

The mean value given by equation (19) is only weakly dependent on the upper bound of integration. That upper bound should be chosen so as to reflect the richness of stellar populations of massive clusters, yet without overwhelming the computational scheme.

The lifetime of a star is a steep function of its mass. We find the following polynomial to give a good fit to stellar lifetimes in the mass range $[5\,\mathrm{M}_\odot, 70\,\mathrm{M}_\odot]$:

$$\log t_{\mathrm{life}} = c_1 \times (\log m)^2 + c_2 \times \log m + c_3, \qquad (20)$$

where $c_1 \approx 0.96$, $c_2 \approx -3.7$ and $c_3 \approx 4.2$; m is expressed in solar masses, and t_{life} in Myr. A star will take full part in the time evolution of the cluster through two-body scattering if its lifetime exceeds the mass-segregation time of equation (10), which we rewrite as (dropping the subscript max)

$$t_{\mathrm{ms}} = \frac{K}{m}, \qquad (21)$$

where

$$K \equiv \frac{\pi}{3}\,\frac{\bar{\rho}}{\rho}\,\langle m \rangle \left(\frac{r_{\mathrm{hm}}}{r_{\mathrm{g}}}\right)^{3/2} t_r. \qquad (22)$$

Combining the two time-scales allows us to find a reference mass to satisfy the relation $\log t_{\mathrm{ms}} < \log t_{\mathrm{life}}$. Substituting t_{life} from equation (20) we obtain

$$0 < c_1 \times (\log m)^2 + (c_2 + 1) \times \log m + c_3 - \log K, \qquad (23)$$

a quadratic inequality for $\log m$. Solving for the roots of this quadratic we obtain

$$\log m^{\pm} = \frac{-c_2 - 1}{2\,c_1} \pm \frac{\sqrt{(c_2 + 1)^2 - 4\,c_1\,(c_3 - \log K)}}{2\,c_1}. \tag{24}$$

The interpretation of this result is straightforward. All stars with initial mass $m \in [m^-, m^+]$ will not migrate much to the centre of the cluster in the course of their lifetime on the main sequence. Those with masses above m^+ and below m^-, will. Therefore, to model accurately the very early stages of clusters we should ideally include all stars above m^+. Recently, Figer (2005) has argued from Arches cluster data that all stars have initially a mass $<150\,\mathrm{M}_{\odot}$: this would set an absolute upper limit on the mass spectrum. However, the impact of such very massive stars on the dynamics is small since they carry a minute fraction of the total mass and luminosity of the system. Thus, the most massive stars we have included in some of the calculations in this paper had $m = 70\,\mathrm{M}_{\odot}$ which already exceeds the mass of Wolf–Rayet stars.

The relation of $m^{\pm}$ to cluster parameters is summed up in the constant K: the fraction of all the stars that will contribute more effectively to mass segregation is, therefore, an implicit function of the cluster we wish to model. The minimum of equation (23) occurs for

$$\log m = -\frac{c_2 + 1}{2c_1} \simeq 1.41, \tag{25}$$

or $m \approx 25.5\,\mathrm{M}_{\odot}$. This is the only root to the quadratic when

$$K = c_3 - \frac{(c_2 + 1)^2}{4c_1} \simeq 200.0 \equiv K_{\mathrm{c}}, \tag{26}$$

where the numerical value follows from our choice of fitting parameters but is otherwise uniquely defined.

The meaning of K_{c} becomes clear if we recall the definition of K and t_{r}, equations (21) and (8). Note first that there are no real roots to equation (23) when $K < K_{\mathrm{c}}$. Whenever that is the case, all stars drawn from the IMF effectively segregate while on the main sequence and lose very little mass in the process. When K exceeds K_{c}, all stars in the interval $[m^-, m^+]$ must evolve significantly on their way to the centre.

But since K increases with the relaxation time t_{r}, itself a rising function of the number of stars N (at a given crossing time), we may work out a value for N beyond which it is unrealistic to neglect stellar evolution. We find after some algebra that the condition $K \geqslant K_{\mathrm{c}}$ reduces to

$$\frac{\bar{\rho}}{\rho} \frac{\langle m \rangle}{\mathrm{M}_{\odot}} \frac{t_{\mathrm{cr}}}{1\,\mathrm{Myr}} \frac{N}{\ln 0.4N} \geqslant 86\,K_{\mathrm{c}}, \tag{27}$$

where we have substituted the numerical factor $r_{\mathrm{hm}}/r_{\mathrm{g}} = 0.4$. Any multimass cluster model (N-body or otherwise) that does satisfy this inequality and neglects the stellar evolution processes is in error. We can isolate for N in equation (27) by taking characteristic values for the crossing time and mean stellar mass to be $t_{\mathrm{cr}} \approx 0.5\,\mathrm{Myr}$ and $\langle m \rangle = 0.7\,\mathrm{M}_{\odot}$. If the stars are not segregated by mass initially then on average $\bar{\rho}/\rho = 1$ by definition. With these values inserted in equation (27) we find $N \geqslant 6 \times 10^5 \equiv N_{\mathrm{c}}$, above the census of an average star cluster in the Galaxy ($\langle M \rangle = 300\,000\,\mathrm{M}_{\odot}$), but not atypical of clusters in the Antennae (Mengel et al. 2002; table 3).

Note that for a given crossing time, a multimass calculation with $N < N_{\mathrm{c}}$ will correctly reproduce the migration of stars up to a time of the order of t_{ms} even without accounting for stellar evolution. Portegies Zwart & McMillan (2002) and Gürkan, Freitag & Rasio (2004) used this argument to model runaway collapse of a cluster leading to the formation of an intermediate mass black hole. To

perform their simulations, they supposed that the relaxation time of their cluster was less than 30 Myr so that collapse occurs before the first stars explode around 3 Myr.

4.1.3 The choice of mass bins

To include very low-mass stars in the computation is costly and brings little in terms of the time-variation of the light curves, cf. equation (10). The difficulty resides in having to resolve the light profile of the high-mass stars, and the potential, dominated by sub-solar mass stars, simultaneously. We mitigated this problem partly by selecting a low-mass cut-off of $0.1\,\mathrm{M}_{\odot}$, well below the mean mass of equation (19). We then defined the mass ensemble $\{m_j\}$, $j = 1, 2, \ldots, J$, such that the lifetimes of two successive high-mass components, m_j, m_{j+1}, differ by ≈ 5 Myr using equation (20). We refer to all stars with initial mass $m > 5\,\mathrm{M}_{\odot}$ as 'massive stars'. In contrast, the sampling of the mass spectrum in the interval $[0.2, 5]\,\mathrm{M}_{\odot}$ followed a geometric mass-doubling progression: $m_1 = 0.2\,\mathrm{M}_{\odot}$, $m_2 = 0.4\,\mathrm{M}_{\odot}$, $m_3 = 0.8\,\mathrm{M}_{\odot}$, etc. We define $m_{1/2} = m_1/2 = 0.1\,\mathrm{M}_{\odot}$. In short, the ensemble $\{m_j\}$ spans the mass range $0.2\,\mathrm{M}_{\odot}$ to m_J non-uniformly and allows a much-improved focus on the evolution of the massive stars.

With mass bins so chosen, the IMF is integrated over each interval $m_{j+1/2} - m_{j-1/2}$ to distribute the mass within each bin j and normalized so that

$$\int_{m_{1/2}}^{m_{J+1/2}} f(m)\,\mathrm{d}m = N. \tag{28}$$

The geometric mean of two successive mass groups has been used to define the bounds of integration ($m_{j\pm1/2}$) for each group (see Fig. 2).

Simulations were done with 7, 14 and 35 mass groups to investigate variations due to a finer sampling of the stellar mass function (see Fig. 3). The trends in mass segregation are robust to decreasing or increasing the number of groups, but are more noisy in calculations performed with on the order of only a few groups. All results in this article are for runs with $J = 35$ mass groups unless stated otherwise.
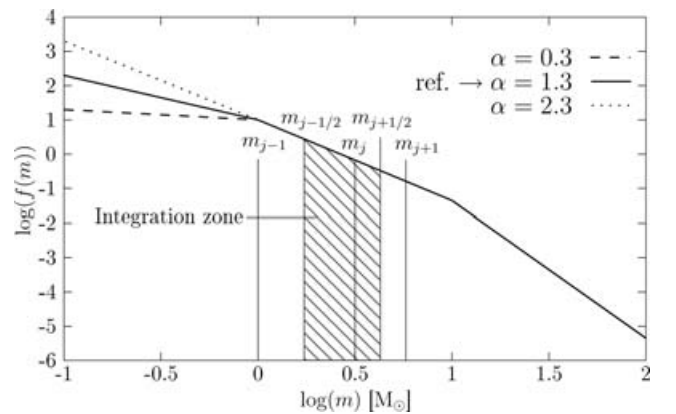

Figure 2. Generic form of the stellar IMF, equation (18). The reference IMF (solid line) corresponds to the power index triplet $(\alpha, \beta, \gamma) = (1.30, 2.35, 4.00)$. Changing α changes the slope on the left-hand side of the figure. The integration algorithm is illustrated for a mass m_j: the integration boundaries are chosen to be the geometric means $m_{j-1/2} = \sqrt{m_{j-1}\,m_j}$ and $m_{j+1/2} = \sqrt{m_j\,m_{j+1}}$ which are mid-logarithmic intervals.
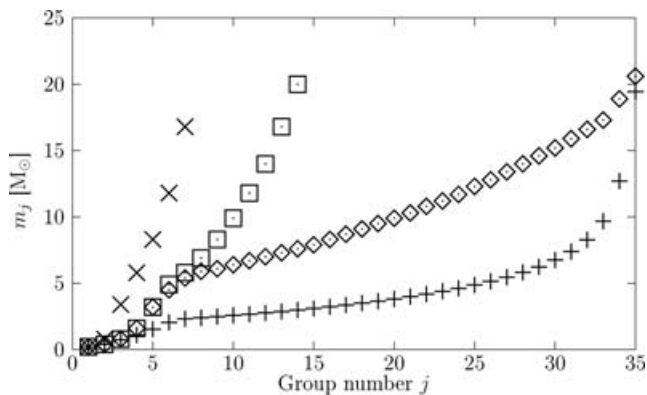
Figure 3. Mean value m_j of each mass group j for simulations with 7 ($\times$), 14 ($\square$) and 35 ($\diamond$) components. The sampling used for the 500 Myr evolution simulation (Fig. 12) is also plotted (+).
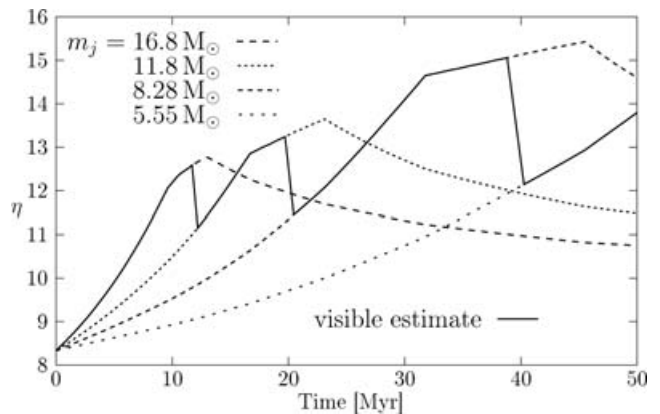

Figure 4. Global η estimated from the brightest of seven mass groups. Dashed and dotted curves show η for each group of mass m_j as indicated. The solid line is the visible estimate for η chosen as the brightest component at any given time. The sudden jumps coincide with the stellar life time of individual groups.

4.2 Radius determinations and Monte Carlo checks

We may distinguish between the half-mass radius derived for the continuous density profile of the gas model, and the same radius derived for an N-body rendition of that continuum.

The half-mass radius for each component of the gas model is computed by integrating once over the entire plane to obtain the total mass of the group; the grid is then resampled to identify the radius R_{hm} enclosing half of the mass. A linear interpolation at the grid points bracketing R_{hm} gives accuracy to second order in the grid interval. Owing to a very fine meshing up to and beyond the half-mass radius, errors on this radius are negligible. In practice, one would like to know what errors are introduced when a finite-N model is projected on the grid and the same radius evaluated from star counts. This is particularly important when the number of stars of a given mass group is low and statistical fluctuations comparatively large.

To that end, we performed two sets of Monte Carlo (MC) tests. First, we computed the half-mass radius for an ensemble of N stars from the surface density of a Plummer sphere projected on the sky. We call the result R_{mc}. Looking at the dependence in N of the fluctuations of R_{mc} around R_{hm}, we concluded that they were of a Poissonian form, mostly due to the random selection of a star in the given density function. For example, with $N = 50$ stars, the dispersion around the mean value is of order 15 per cent, for $N = 1000$, it is 3 per cent. Second, we perform 1000 MC realizations of the 500 000 stars reference model (see Table 1) using the density functions at 10 and 40 Myr to see which are the dispersions of the fluctuations on the mean value of the half-*light* radius. In both case, the dispersion was of order 3 per cent assuring that in a real cluster of half a million stars the half-*light* radius is dominated by the 1000 or so (i.e. 0.2 per cent) most luminous stars.

4.3 Predominant group approximation

Following the latter remark, and in order to have a better understanding of what is going on, we decided to restrain our measures to the most luminous component whose half-mass radius and velocity dispersion are assumed to be the measured half-light radius R_{hl} and velocity dispersion σ_{los} of the whole cluster.

Fig. 4 graphs η for each individual group (thin lines) and the brightest stars (thick solid line). The individual thin curves all increase from their value at $t = 0$. The increase is steeper for the most massive stars, as expected. At $t \approx 10$ Myr, these stars become supernovae and turn to faint stellar remnants thereafter. The η we compute for the system drops sharply to the underlying value given by the new most-luminous stellar population. And so on for each subsequent episode of mass-loss (ML) through supernovae events. Note that at later times the η of individual stellar groups decreases as a result of significant ML. This trend is again driven by mass segregation, when the lighter remnants are expelled from the central region by the massive stars. Such remnants behave like point sources of gravity with no further stellar evolution. The trend where η decreases is caused mainly by an increase of the half-mass radius, which is more significant than variations in velocity dispersion.

The value of η computed from the most luminous component gives an upper limit on the value of η derived from the integrated light of all stars. An illustration based on bolometric light will be discussed in Section 6.3 (Fig. 12). Note that the difference between the two values depends on the wavelength of observation. At the near-infrared wavelengths often used to study highly reddened starburst clusters, both values of η are essentially identical as soon as the most massive stars have evolved off the main sequence. Indeed,

Table 1. Parameters and useful data for the reference Plummer model. J is the total number of groups, N the number of stars, M the initial total mass. R_{hm0}, σ_{los0} and η_0 are, respectively, the initial half-mass radius, line-of-sight velocity dispersion and η. $\Sigma(0)$ is the central surface density of the cluster, t_r and t_{ms} its relaxation and segregation times. Note that for $J = 35$, we have $m_{1/2} = 0.1\,M_\odot$ and $m_{35+1/2} = 20.6$. We also have $m_{min} \equiv m_1$ and $m_{max} \equiv m_{35}$. The indexes α, β and γ define the IMF (see equation 18). The eight parameters on the left-hand side are adjustable in the code whereas the six on the right-hand side are derived from them.

								Adjustable quantities					Derived quantities	
J	N	R_{hl0} (pc)	m_{min} ($M_\odot$)	m_{max} ($M_\odot$)	α	β	γ	M ($M_\odot$)	σ_{los0} (km s^{-1})	η_0	$\Sigma(0)$ ($M_\odot$ pc^{-2})	t_r (Myr)	t_{ms} (Myr)
35	500 000	1	0.2	20.0	1.30	2.35	4.00	418 000	15	8.6	0.67×10^5	180	2

short-lived red supergiants or asymptotic giant branch (AGB) stars overwhelm other sources of light; at each time, their distribution is that of the currently most massive objects.

4.4 Number of components

The large oscillations seen in Fig. 4 for a model with $J = 7$ components suggested to us to aim for a significantly larger sampling of the mass function to reduce noise to acceptable levels. Boily et al. (2005) had found for a different reference model that $J = 14$ already gave enough precision to identify global trends. Some uncertainties remain with $J = 14$ models in the later stages of evolution and in particular when the evolution time exceeds 100 Myr. This suggested to us to increase J to the largest possible value. The computational time however is quadratic in J and so after some experiments, we settled for a compromise value of $J = 35$ mass groups binned inhomogeneously as described in Section 4.1. The difference between $J = 14$ and 35 models lies mainly in a much smoother transition at the time when the massive stars undergo rapid ML while the dynamics for the same mass-component is less affected.

5 PARAMETER SURVEY

We now survey different parameter values for N, m_{max}, R_{hm0} and $\langle m \rangle$. We tried in each comparison to maintain all but one parameter fixed to the reference model values given in Table 1. From equations (10), (8) and (4) coupled with equation (1) to eliminate σ, we get

$$t_{ms} \propto \frac{\langle m \rangle}{m_{max}} \frac{N}{\ln(0.4\,N)} \frac{R_{hm0}}{\sqrt{\langle m \rangle\,N/R_{hm0}}}$$

$$\propto \frac{\sqrt{\langle m \rangle\,N\,R_{hm0}^3}}{m_{max}\,\ln(0.4\,N)}. \tag{29}$$

The survey will highlight dependencies of t_{ms} on each quantities. In all the graphs that follow the solid line indicates the reference model of Table 1 unless stated otherwise.

5.1 Particle number

We first investigate the behaviour of η when changing the total number of stars, N while the initial half-mass radius R_{hm0} is kept unchanged. The number N of the survey ranged from 4 to 15×10^5 stars. These values of N bracket the clusters of mass equal to the mean mass of Milky Way clusters (some $300\,000\,M_\odot$; Meylan & Heggie 1997) and the very rich Antennae clusters of more than $10^6\,M_\odot$ (e.g. Mengel et al. 2002). The models all have identical mass groups and upper-mass limit. With the main sequence lifetime of $20\,M_\odot$ stars $\approx 10\,$Myr we expect from equation (29) a more segregated profile and larger η at that time for smaller-N systems, and a similar trend in evolution thereafter. Fig. 5 graphs η for five values of N in the range indicated. It is clear from that figure that richer clusters, with a longer segregation time, show a less-rapidly changing η. This situation carries over beyond $t \approx 10\,$Myr when the first supernovae events occur, as the second most heavy stars continue to converge to the centre on their own segregation time-scale, also $\propto \sqrt{N}$. As a result, the mass profiles are less segregated when the stars move off the main sequence in succession for runs with higher values of N. Overall differences in the profiling of η at times $t > 10\,$Myr remains small: for instance the average slope $d\eta/dt$ is ≈ 1.20 for the $N = 1.5 \times 10^6$ model, and ≈ 1.31 for the smallest-N model shown here. The differences are without major implications if we are concerned with clusters of ages $<100\,$Myr or so.
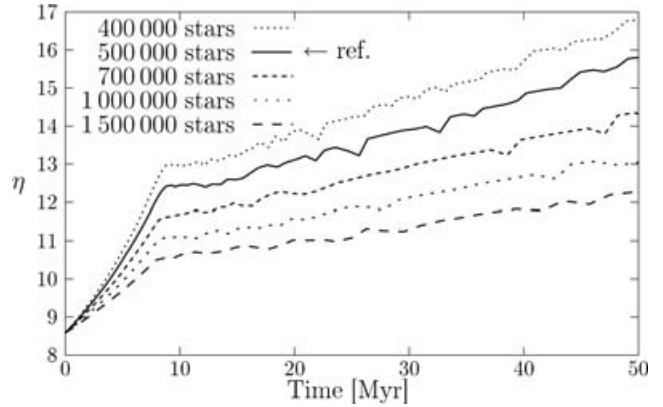

Figure 5. Evolution of η for different total number of stars N. Note the very similar slopes of the curves at times $t > 10\,$Myr. The stellar IMF was truncated at $20\,M_\odot$.

5.2 Non-monotonic evolution?

Large-N clusters will host a very rich stellar population and very massive stars. These stars have very large luminosity but are extremely short lived; their impact on the value of η should therefore be more significant on short time-scales. It is interesting, then, to follow the behaviour of η for individual components when the mass spectrum includes heavy stars easily identifiable from spectroscopy which could be taken as tracers for the global dynamics. A tracer might be the brightest stellar component at any given time and we have seen how η can be estimated from the brightest component alone (Fig. 4). Would η increase monotonically in time if such a tracer was used instead of a global value obtained from integrated light? Call η_j the value of η computed for a single component $j = 1, 2, \ldots, J$, of mass m_j, and main-sequence lifetime $t_{life\,j}$. The mass of the brightest star is a monotonically decreasing function of t and if j is the brightest mass group at time t then we would say $\eta = \eta_j$.

From basic stellar evolution models we have $t_{life\,j+1} < t_{life\,j}$, and so $\eta = \eta_j$ in the time interval $t_{life\,j+1} < t < t_{life\,j}$. Thereafter $\eta = \eta_{j-1}$, and so on. We noted that η is a growing function of t/t_{ms} while the stars are on the main sequence. Hence, to find out whether η will increase or decrease as we switch from η_j to η_{j-1}, it is sufficient to check whether t_{life}/t_{ms} is a decreasing or growing function of stellar mass. In Section 4, we fitted the logarithm of t_{life}/t_{ms} with a quadratic function of $\log m$, equation (25). We found a minimum for the quadratic (i.e. $\log t_{life}/t_{ms}$) at $m \approx 25\,M_\odot$. Therefore, if the current brightest stars have a mass that is larger than $25\,M_\odot$, we should find $\eta_{j-1}(t_{life\,j-1}) < \eta_j(t_{life\,j})$. On the contrary, if the current brightest mass is $< 25\,M_\odot$, then $\eta_{j-1}(t_{life\,j-1}) > \eta_j(t_{life\,j})$ and hence $\eta(t)$ measured from tracers would increase with time.

We graph in Fig. 6(a) the curves of $\eta = \eta_j$ for different cut-offs of the mass function, ranging from 12 to $70\,M_\odot$. It is clear that very large-mass tracers completely bias the value of η to large values, however they can only do so for very short times running up to $\approx 10\,$Myr. We note that η_j is non-monotonic with time for a cut-off exceeding $25\,M_\odot$, as expected. The mass of a star cluster derived from massive stellar spectroscopic tracers ($>30\,M_\odot$) is off by a factor that can exceed ≈ 2 for the reference set-up (Table 1). Note, however, that at $t \approx 10\,$Myr and later, all the curves fall back on the same profile, to within small fluctuations. For comparison, we plot in Fig. 6(b) the solid curve of Fig. 6(a) along with the evolution of η_{lum}, the analogue of η computed from light-weighted integrated
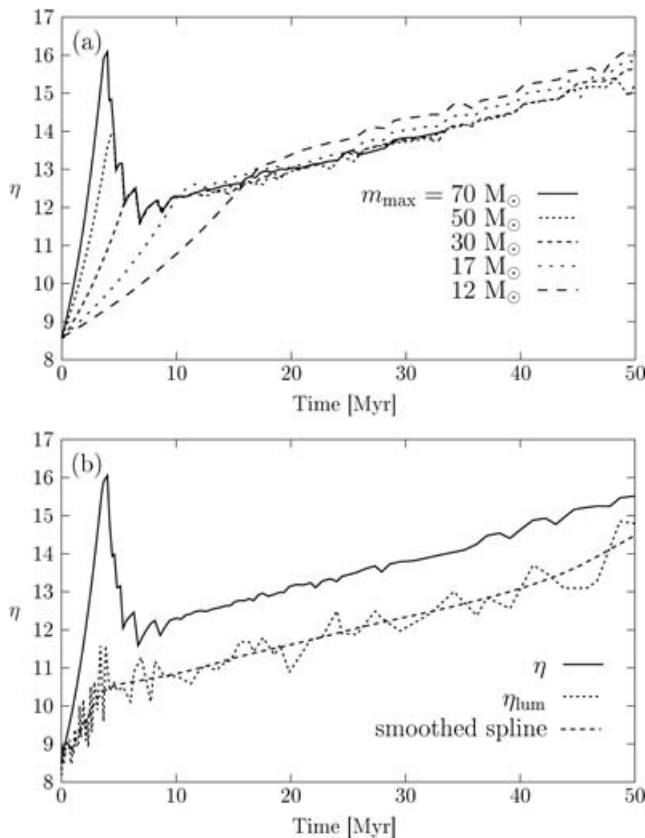
Figure 6. Evolution of η for models with different upper-mass cut-off $m_{\max}$. (a) We set $\eta = \eta_j$ of the brightest component at time t (see Section 4.3). When the stellar mass function is extended beyond $M = 25\,M_\odot$, η_j is not monotonic and becomes rapidly very large at early times. (b) Same as (a) for $m_{\max} = 70\,M_\odot$ (solid line) and η_{lum} computed from summing the light from all the stars at all times for the same model (dotted line). Note that the first 'bump' due to an extended mass range is much attenuated when computed with total bolometric light curves from MC sampling. The effect of very bright and short lived stellar states (e.g. AGB) cause many oscillations due to the random sampling in the profile of η_{lum}.

Figure 7. Evolution of η for models with different projected initial half-mass radius R_{hm0}. The denser models have smaller radius. Note that the low-density model with $R_{\mathrm{hm0}} = 2.0\,\mathrm{pc}$ shows hardly any evolution.

Fig. 7 for five values of projected initial half-mass radius, from 0.5 to 2 pc. The low-density model with $R_{\mathrm{hm0}} = 2\,\mathrm{pc}$ has a central density $\approx 2 \times 10^4\,M_\odot\,\mathrm{pc}^{-2}$ and we find an increase in η of at most 20 per cent after 50 Myr of evolution; by contrast the model with $R_{\mathrm{hm0}} = 1/2\,\mathrm{pc}$ of central density $\approx 3 \times 10^5\,M_\odot\,\mathrm{pc}^{-2}$ shows a dramatic increase of η by a factor $\approx 30/8.6 = 3.5$ in just 10 Myr of evolution. The rapid increase of η is driven by the much shorter dynamical time of the compact cluster which trickles down to a shorter t_{ms} in equation (29): $t_{\mathrm{cr}} \propto R^{3/2}$ implies a segregation time $4^{3/2} = 8$ times shorter for that model compared with that of the low-density run.

5.4 Stellar IMF: $\langle m \rangle$

There is much on-going debate concerning the universality of the stellar IMF. The shape of the IMF will fix the mean stellar mass which enters the definition of the segregation time in equation (29). We already noted that stars at the high end ($>10\,M_\odot$) of the mass spectrum carry much light individually but unless their numbers are greatly enhanced contribute a small fraction of the total mass. In our exploration of the impact of the shape of the IMF on the dynamics, we have therefore kept the index $\gamma = 4.0$ as for the reference set-up (Table 1), and focused instead on the effect of varying the low-mass power index α. As most of the cluster mass is in low-mass stars, α dominates the mean mass value and bears directly on η. The same mass range and number of groups were used in all cases discussed below.

Fig. 2 illustrates the three different IMFs used to perform the simulations plotted in Fig. 8. To encompass the standard errors of ± 0.7 (Kroupa 2002), we varied our parameter α by ± 1. The chosen upper value $\alpha = 2.3 = \beta$ ($\langle m \rangle = 0.47\,M_\odot$) corresponds to a Salpeter profile; it is reasonable to assume that any stellar IMF must flatten out at the low-mass end to avoid a divergence in mass. When we do reduce α to 0.3 ($\langle m \rangle = 1.3\,M_\odot$), the shift in the evolution of η is at no time as dramatic as the one for the Salpeter value. Flattening the IMF below the reference $\alpha = 1.3$ profile has not a significant effect on η.

6 OBSERVATIONAL IMPLICATIONS AND LONG-TERM EVOLUTION

6.1 The stellar mass function

The shape of the stellar mass function might be expected to vary with radius as a result of mass segregation. The central region is rapidly

quantities rather than just from the most luminous component. In practice, η_{lum} is calculated using MC representations of the simulated clusters. Clearly, the bolometric $\eta_{\mathrm{lum}} < \eta$ at all times, as anticipated from Section 4.3. If a red filter were applied, η_{lum} would be weighted predominantly by red giant stars, the brightest population, and hence the gap between the two curves would close up. The time derivative at $t \gtrsim 10\,\mathrm{Myr}$ is almost unchanged, so that the trends in time that we will derive in a forthcoming section applies to either η.

5.3 Mean density via R_{hm0}

Observed clusters in M82 or the Antennae are compact. They show averaged surface densities that may exceed the reference value $\approx 7 \times 10^4\,M_\odot\,\mathrm{pc}^{-2}$ that we have adopted. Boily et al. (2005) already noted that the evolution of η is significant only for clusters with surface density exceeding $\sim 10^4\,M_\odot\,\mathrm{pc}^{-2}$ (at constant number of stars). In another context, it is known that the mass density of galactic nuclei may well exceed $10^7\,M_\odot\,\mathrm{pc}^{-3}$.

We have therefore explored the evolution of clusters with different central surface densities by multiplying lengths by a factor chosen to cover more than a decade in density. The results are plotted in
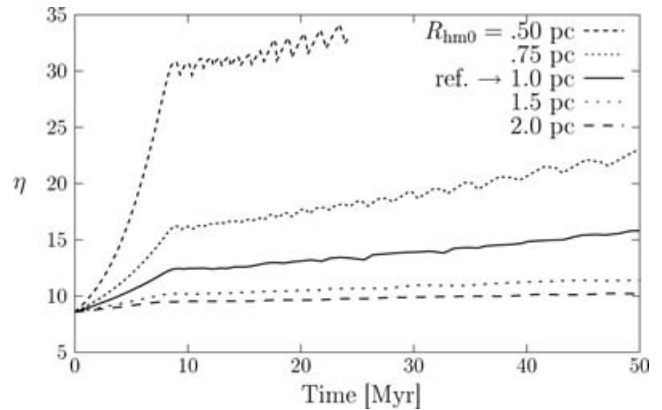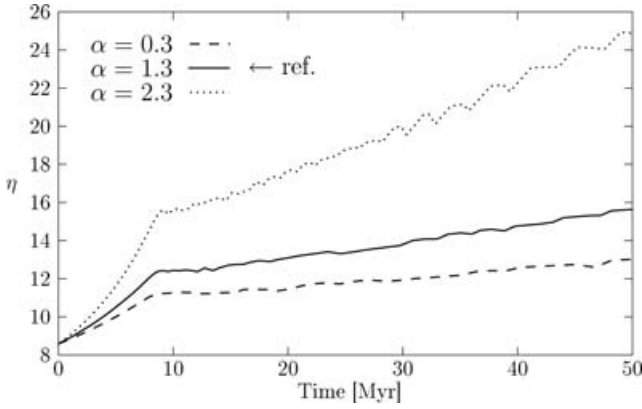
Figure 8. Evolution of η for the reference model with different low-mass power index α for the stellar IMF (see Fig. 2). The mean mass are $\langle m \rangle = 1.3, 0.85$ and $0.43\,M_{\odot}$, respectively, for $\alpha = 0.3, 1.3$ and 2.3.

overstaffed with high-mass stars while the outer parts are depleted of them. This trend can be quantified through the power indices α, β and γ of the mass spectrum, by comparing the mass function inside and outside a reference radius. Unfortunately, a cluster evolving rapidly in time offers no fixed reference radius. To palliate this, we computed the stellar mass function in two concentric surface elements bounded by the half-light radius from the most massive group. While not specially meaningful, this choice offers the advantage of a direct link with an observable quantity.

From the star counts in each of the 35 mass bins, the mass function is retrieved by summing all the mass within m and $m + \mathrm{d}m$, and dividing by $\mathrm{d}m$ to obtain a density. We then least-squares-fitted power laws in the ranges $[0.1; 1\,M_{\odot}]$, $[1\,M_{\odot}; 10\,M_{\odot}]$ and $[10\,M_{\odot}; 20\,M_{\odot}]$ as in Table 1. Since the binning is not at constant width, we worried that the mass discretization would introduce large errors in the values of the power indices retrieved. To check this, we trained our algorithm on the known IMF from star counts at $t = 0$ for the reference as well as a coarser binning: the power indices α, β, γ of Table 1 were recovered to ± 0.01, which we take as s.d. values.

Fig. 9 compares the initial mass function (solid line) with the mass function derived inside (dashed line) and outside (dotted line) the half-light radius at three different times. With the standard model, the changes in the mass function are small, therefore the model cluster in this section was initially twice as concentrated ($R_{\mathrm{hm0}} = 0.75$ pc) as the reference Plummer model ($R_{\mathrm{hm0}} = 1$ pc) but otherwise the same. The three curves are trivially identical at $t = 0$ with slopes given by the Kroupa IMF. As time increases, the low-mass power index α remains virtually unchanged in the outer region (varying from 1.3 to $\simeq 1.33$) but shows a noticeable decrease in the inner part of the system, down by ≈ -0.25 after 75 Myr of evolution. The power index β for the mass range $[1\,M_{\odot}; 10\,M_{\odot}]$ shows the strongest variations of all, down from its initial value by as much as -1 inside the half-light radius, and up by $+0.4$ outside this radius. The steeper slope in the outer region is a direct consequence of the outward migration of light stars initially inside the half-light radius, while heavy stars flow in the opposite sense.

For very massive stars, the situation is made slightly more complicated by the fact that the life-time of these stars is comparable to, or less than, the evolution times displayed in Fig. 9. The vertical straight line on each panel indicates the mass for which the life-time equals the time displayed. All stars to the right-hand side of this line are low-mass remnants from, for example, supernovae
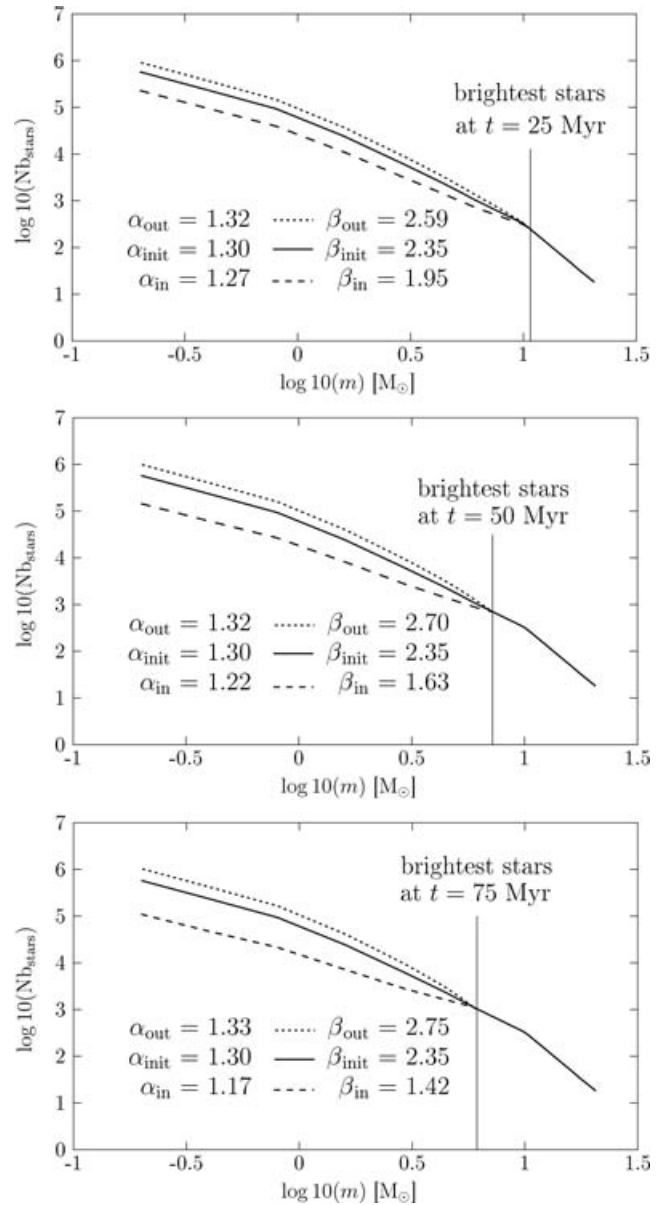

Figure 9. The mass function after 25, 50 and 75 Myr of evolution for a Plummer model of initial projected half-mass radius 0.75 pc (other parameters as in Table 1). The vertical line indicates the brightest group of stars on each panel. The mass function has been retrieved, first by computing the projected half-mass radius of the brightest component, and then by binning stars inside and outside that radius at each t (see text for details). The slopes α and β were obtained by linear regression of the data on the left-hand side of the vertical line.

events: these stars therefore do not contribute to the light profile of the cluster. Stars initially in this mass range are now contributing a small addition to the census at the low-mass end of the distribution. The high-mass part of the diagram is therefore completely depleted, and has not been fitted.

These trends with radius are similar to those measured in young LMC clusters such as NGC 1818 (Hunter et al. 1997; de Grijs et al. 2002b; Gouliermis et al. 2004). This cluster has an age of ~30 Myr falling between the times displayed in Fig. 9 and a calculated relaxation time ~250 Myr assuming a half-mass radius of 2.6 pc and mass of $30\,000\,M_{\odot}$ (de Grijs et al. 2002a) with $\langle m \rangle = 0.85\,M_{\odot}$.

This is longer than in our simulations. Note however that the mean density of the model with $R_{hm} = 0.75\,pc$ matches well the density inside the half-mass radius of the cluster NGC 1818 (Elson, Fall & Freeman 1987). Inspection of Fig. 9 of Gouliermis et al. (2004) shows that the power indices in the inner part (e.g. <0.3 arcmin) derived from their data are similar to those of our simulation. This raises the possibility that *dynamical* mass segregation may yet play a key role at the heart of that cluster while *primordial* segregation is needed to explain the external parts, a conclusion already reached by de Grijs et al. (2002b).

6.2 Colours

It is interesting to investigate to a fuller extent observable consequences of mass segregation. To that end, we extracted colours from our model clusters by coupling the Cambridge evolution tracks to the spectral library of Lejeune, Cuisinier & Buser (1997, 1998). Nebular gas emission lines, thought present in embedded young clusters (Anders & Fritze-v. Alvensleben 2003), are left out of the current analysis.

Sampling the mass spectrum requires some care in order to minimize errors in colour magnitudes as discussed by Charlot & Bruzual (1991). First, we tabulated the various evolutionary epochs for a large set of masses split in equal logarithmic intervals from 2 to $100\,M_\odot$. The luminosity function was constructed by carefully integrating the light flux from all the stellar masses in a given evolution phase, paying great attention to resolve such brief but very bright phases as the upper AGB.

Colours were computed in different wavebands (B,V,I from Bessell 1990, and K from Bessell & Brett 1988) and compared with those of other authors, who used the evolutionary tracks of the Geneva group, the Padova group or variations thereof (Girardi & Bertelli 1998; Bruzual & Charlot 2003; Mouhcine & Lançon 2003 and references therein; mostly based on tracks by Bressan et al. 1993 or Schaller et al. 1992). We found that the Cambridge tracks produce significantly redder colours than others, which have in general been more specifically tuned to reproduce the observed integrated colours of star clusters. The origin of these differences lies in the time stars spend in the late, red phases of stellar evolution. In calculations using the Cambridge tracks, the predominance of red supergiants and upper AGB stars at near-infrared wavelengths is probably exaggerated. To illustrate the effect of the luminous red stars, we ran simulations with and without stars on the thermally pulsing AGB (TP-AGB). Fig. 10 shows the evolution of the integrated $V - K$ colour of the model cluster. The two curves bracket values commonly found in the literature for simple stellar populations.

Colour gradients were quantified by measuring the difference between the colours measured inside and outside the projected half-light radius:

$$\Delta_{V-K} \equiv (V-K)_{<R_{hl}} - (V-K)_{>R_{hl}}. \tag{30}$$

$\Delta_{(V-K)}$ is positive when the inner half of the cluster is redder than the outer half. Fig. 11 shows the evolution of Δ_{V-K} for the reference model (Table 1). At early times, mass segregation tends to make the centre bluer, as the massive stars that fall towards the centre are still on the main sequence. Once these stars evolve off the main sequence, the centre of the cluster very rapidly becomes the reddest part. Further evolution of the colour gradient presents fluctuations that reflect the lifetimes of stars of progressively smaller initial masses and the mass-dependent time they spend as luminous red objects. However, Δ_{V-K} remains above 0.05 mag
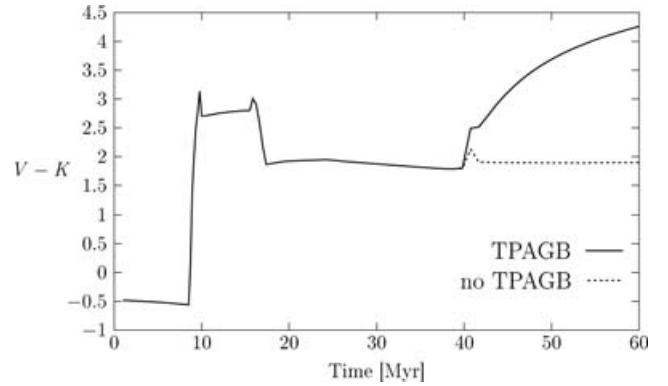

Figure 10. $V - K$ plotted against time for the reference model cluster (see Table 1). The solid line is for integration with all possible stellar phases including the TP-AGB. The dotted line is the same but without the TP-AGB phase.

throughout, even when the brightest stars such as those of the TP-AGB are artificially switched off.

6.3 Long-term evolution

It is natural to ask whether the continued increase of η observed for the reference model over a time-scale of $\sim$100 Myr carries over to longer time-scales. Recall that the relaxation time of that model $\sim$200 Myr from equation (8). We would anticipate some increase in η for any cluster with an age $\gtrsim t_r$, however longer relaxation times also imply longer mass-segregation times and significant contributions from low-mass stars to η. Since the stellar winds of lower-mass stars moving off the main sequence are less energetic, it is not clear whether or not the residual gas will be evacuated on a very short time-scale and how this will impact on the dynamics. We take the view that much of the gas can either remain within the cluster for a period exceeding t_r, or on the contrary be evacuated rapidly, thus
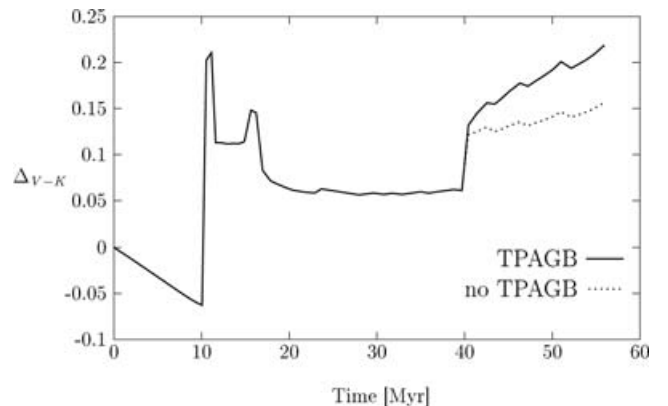

Figure 11. Difference of colour Δ_{V-K} between internal and external part of a cluster relative to its half-light radius at each given time. The inner region becomes bluer over the first 10 Myr of evolution, when the most massive stars in the sample ($m_{max} = 20\,M_\odot$) become red giants. Thereafter, the inner part remains systematically redder than the outer region by as much as 0.2 dex over the first 50 Myr. Note however that the colour index Δ_{V-K} fluctuates wildly. The trend of increasing Δ_{V-K} at $t > 40$ Myr is continued in time exceeding 60 Myr (off scale). To account for possible bias from the TP-AGB phase, when stars are very bright in the red, we recomputed the colours by removing all stars in that phase of evolution (dotted line on the figure). The behaviour stays unchanged.

hopefully bracketing all realistic cases. Below we assess whether either limit (or both) will result in a drop in η over long time-scales.

We ran the reference calculation (Table 1) for up to 500 Myr. That stretch of time would correspond to several revolutions through the galactic potential of a galaxy such as the Milky Way, and overrun the starburst phase of a typical galaxy merger where young clusters are observed to form. Since heavy stars play only a minor role beyond $\sim$30 Myr of evolution (cf. Fig. 6), we split the 35 mass bins so that the stellar MS lifetimes now differ by $\approx$20 Myr from one bin to the next (instead of five adopted earlier, see Fig. 3). In this way, the part of the mass spectrum below $5\,M_\odot$ is far better sampled than previously. Nevertheless, the discreteness of the mass function will cause large fluctuations, particularly noticeable at times $t \gtrsim 200$ Myr (cf. Section 4.3) and tend to underestimate the increase of η as we have seen when comparing simulations with fewer components.

In Fig. 12, we graph η evaluated in three different ways for comparison. The dotted curve (denoted 'η with ML') assumes instantaneous evacuation of the mass released through stellar evolution. The dashed curve denoted $\eta_{\rm lum}$ also assumes instantaneous mass evacuation but is the analogue of η computed (as in Fig. 6) from light-weighted quantities, using a MC representation of the cluster. To verify the impact of stellar ML, we also plot the value of η obtained with a constant total cluster mass. The result is shown in Fig. 12 labelled as 'η without ML' (solid line). For that curve we find an increase of η of a factor ranging from 5 to 6 by the end of the run. This curve remains significantly and systematically higher than the other two throughout the run. These curves bound, therefore, all possible values because in practice some of the gas will leak out and $\eta \propto M$ would decrease as a result. A full simulation including hydrodynamical effects would trace η somewhere between the curve shown here for $\eta_{\rm lum}$ and the solid line of η without ML.

It is highly likely that tidal fields will affect the morphology of a cluster as it orbits the host galaxy. This will certainly change the profiling of η in time, for example, by stripping some of the cluster mass. But unless the cluster evolves in a very strong tidal field, the
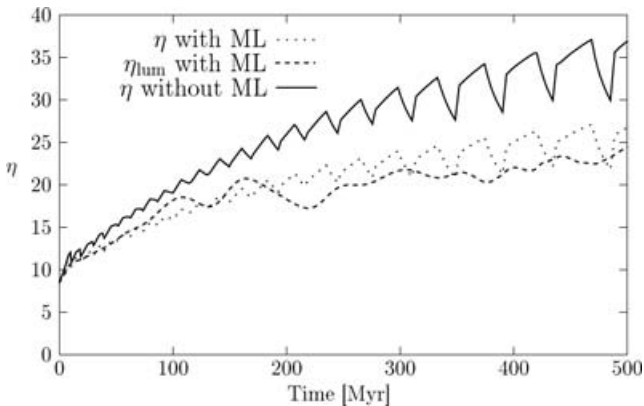
dynamics inside the half mass radius should prove relatively robust. If the total cluster mass decreases, stripping mass outside $r_{\rm hl}$, then η would decrease from the values obtained here. A full inspection of this issue would require three-dimensional model clusters which lay beyond the scope of the current study.

7 APPLICATION TO CLUSTER MASS FUNCTIONS (CMFs)

7.1 η–$t_{\rm r0}$ relation

The results of Sections 5.1 and 5.3 suggest a common thread linking models of high mean density and those of smallish total mass. Since these two quantities combine to give the system relaxation time in equation (8), we may hope to relate η for models of different relaxation times but comparable ages for a given IMF through a simple scaling formula involving the initial relaxation time $t_{\rm r0}$. Thus, we take the view that evolution will be driven almost exclusively by two-body relaxation and not, for example, variations in the stellar mass function. Such effects would play a significant role, as shown in Fig. 6, but only for clusters not older than a few Myr.

We sought out such a scaling relation by performing a series of runs for models with different values of $t_{\rm r0}$, spanning a wide range of values in $R_{\rm hm0}$ and N but in other respects identical to the reference model (Table 1). We computed η for these models at $t = 10$ Myr, approximately when the first stars become supernovae, and a time $t = 40$ Myr which gives an intermediate age between, for example, age estimates of Antennae clusters (Mengel et al. 2002) and that of M82-F (Smith & Gallagher 2001; McCrady, Graham & Vacca 2005). Fig. 13 plots the variations in η at these two times relative to its initial value, $\Delta\eta_t/\eta_0$, as function of $t_{\rm r0}$. Both sets of points are well fitted by single power laws,

$$\frac{\Delta\eta_t}{\eta_0} = A_t \times t_{\rm r0}^{-a_t}, \tag{31}$$

and we list the values of A_t and power index a_t in Table 2 for two different times. The error bars shown on the figure result from oscillations of η due to the mass sampling. The power index a_t shows only a mild dependence on the age of the cluster. This is somewhat surprising if we note that the same power-law functional fit applied to the half-light radius $\Delta R_{\rm hl}/R_{\rm hl0}$ and square velocity dispersion $\Delta\sigma_{\rm 1d}^2/\sigma_{\rm 1d0}^2$ give equally good results but now the parameters vary much between the two chosen times (cf. Table 2).
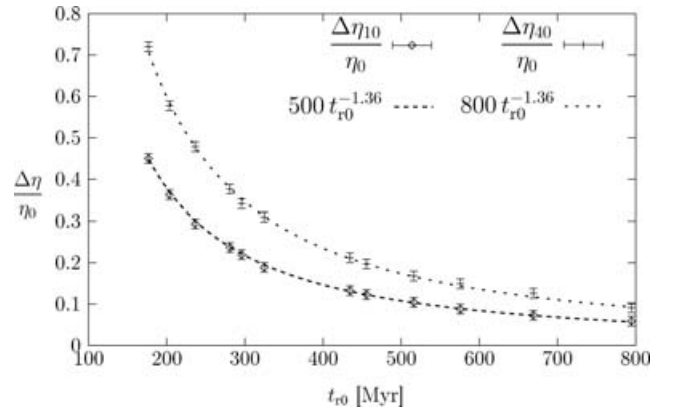

Figure 12. Parameter η versus time for an 35-component simulation (see text for details of the numerical set-up). The top-most solid curve was obtained by computing η at constant total cluster mass, so disregarding ML due to stellar winds. The dotted curve assumes on the contrary that this ML leaves the cluster instantaneously. A more realistic situation where the stellar winds escape over a finite time interval would pitch η somewhere between the two curves shown here. Note that η was once more calculated by taking the most luminous component as tracer. If we draw MC realizations using the luminosity from all the stars to compute $\eta = \eta_{\rm lum}$ under the same assumption of instantaneous ML, we instead obtain the dashed curve which shadows closely the dotted line. Either way of computing η yields continued increase up to 500 Myr.

Figure 13. The parameter η as a function of initial relaxation time $t_{\rm r0}$ from different simulations where both N and $R_{\rm hm0}$ have been varied. The relative increase $\Delta\eta/\eta_0$ is a power law of $t_{\rm r0}$. The error bars are deviations from the mean value of η at each time.

Table 2. Power-law fits to η as function of the initial relaxation time. A least-squares fit of the functional form defined by equation (31) was performed at two cluster ages. The s.d. values on A_t and A_t are, respectively, 5 and 1 per cent.

	$t = 10\,\mathrm{Myr}$			$t = 40\,\mathrm{Myr}$		
	η	R_{hl}	$\sigma_{1\mathrm{d}}^2$	η	R_{hl}	$\sigma_{1\mathrm{d}}^2$
A_t	500	−90	−57	800	−76	−36
a_t	1.36	1.15	1.22	1.36	1.05	1.08

A general expression for η valid at ages between 0 and about 50 Myr can be derived from the above. Guided by the aspect of Figs 5, 7 or 8, we distinguish an early regime of rapid evolution, up to $\sim$10 Myr, and a subsequent regime of slower changes. A good fit to model values is obtained by running a straight line from the value of η at $t = 0$ to its value at $t = 10$ Myr for the early regime, and another straight line through the values at 10 and 40 Myr for the later evolution, using Table 2. It can be summarized, with t in Myr,

$$\begin{cases} a_t = 1.36, \\ A_t = \begin{cases} 50\,t & \text{if } t < 10 \text{ Myr}, \\ 10\,t + 400 & \text{if } t > 10 \text{ Myr}. \end{cases} \end{cases} \tag{32}$$

Fig. 14 compares the analytical values with the results of a simulation with $t_{\mathrm{r0}} \simeq 205$ Myr. Differences do not exceed 10 per cent even when extrapolating to ages of $\sim$100 Myr. This level of error is found for all models with an initial relaxation time above 100 Myr. When the relaxation time is shorter, we find that the interpolation scheme systematically underestimates η.

7.2 Application to a model CMF

Using the linear interpolation scheme of the preceding paragraph we may compute the current mass conversion factor η of a cluster from equation (31) given t_{r0} and its age $t < 100$ Myr. The real mass of the cluster so retrieved may then be compared to the mass estimate we would have computed had we kept the initial value $\eta_0 \approx 8.6$ constant throughout; the ratio of real to estimated mass equals $\eta(t_{\mathrm{r0}}, t)/\eta_0$. To compute $\eta(t_{\mathrm{r0}}, t)$ first requires a cluster mass and half-mass radius, in order to evaluate t_{r0} from equation (8). To do this for an ensemble of clusters, we set up Gaussian distributions
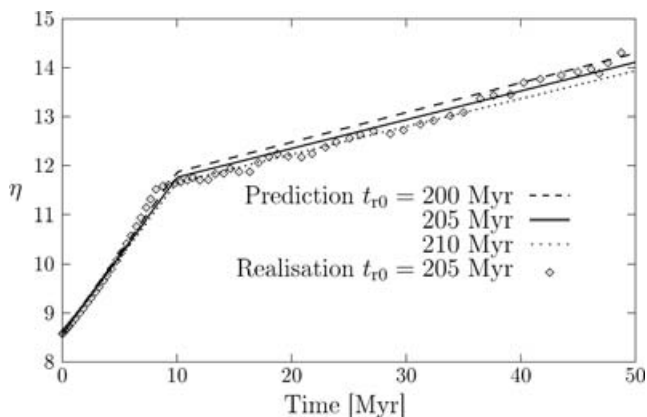

Figure 14. Example of the reconstruction of the evolution of η in time. The symbols ($\diamond$) represent the data from the model while the various curves are drawn from the parameter fits of Table 2 using three values of t_{r0} in equation (31).
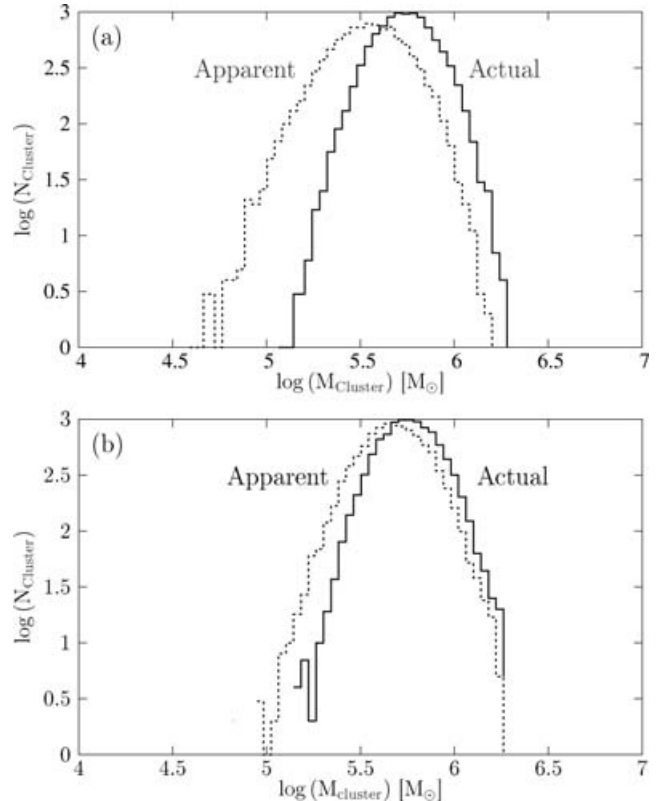

Figure 15. Apparent (dotted curves) and actual (solid curves) cluster mass functions drawn from Gaussian distributions in radii and ages. (a) Results for a cluster mass distribution of mean radius equals 1 ± 0.2 pc and mean age equals 30 ± 5 Myr; and (b) same as (a) but with mean radius equals 2 ± 0.4 pc and mean age equals 60 ± 10 Myr. The MC realizations contained 10 000 clusters. The resulting distribution of initial relaxation time are (a) 190 ± 70 Myr and (b) 550 ± 130 Myr.

for M and R_{hm} as well as the cluster age, t. These distributions were each sampled independently with 10^4 realizations using a standard Ulam–von Neumann (MC) rejection method. In the following, we quote the dispersion σ of these distributions as uncertainties on the mean value (i.e. mean $\pm\,\sigma$).

The results are shown in Fig. 15 with a log-Gaussian CMF of mean mass 5×10^5 M$_\odot$ for two realizations: (a) an ensemble of compact clusters of mean radius 1 ± 0.2 pc and age 30 ± 5 Myr, in line with values adopted for our reference model and (b) an ensemble of mean radius 2 ± 0.4 pc and mean age 60 ± 10 Myr inspired from M82-F cluster data (McCrady et al. 2005). The resulting relaxation time distributions are, respectively, 190 ± 70 Myr and 550 ± 130 Myr.

Because the mass derived assuming a constant $\eta = \eta_0$ is always lower than the actual cluster mass, the distribution shifts to lower masses as compared to the true CMF. Table 3 list the displacements of the peak of the CMF for four Gaussian distributions of different mean initial relaxation times t_{r0}, each of the same 50 Myr dispersion. It is clear that the shorter relaxation times lead to a larger shift and we find a maximum shift of 0.2 dex for the distribution of average $t_{\mathrm{r0}} = 150$ Myr. Very similar conclusions apply for the ensemble of longer-relaxation time when the average age is also longer [case (b) above, displayed on the right-hand panel in Fig. 15].

In this spirit, the very massive and young Antennae clusters are particularly interesting. Table 3 of Mengel et al. (2002) lists parameters for five young clusters of ages ranging from 6 to 10 Myr and

Table 3. Shift of a lognormal distribution in mass centred on $10^6 \, M_\odot$ for different mean relaxation times. The cluster population has a Gaussian age distribution of mean 30 ± 20 Myr.

$\langle t_{r0} \rangle \pm 50$ Myr	150	250	350	450
Shift of $\langle \log M \rangle$	0.2	0.15	0.1	0.05

masses from 600 000 to $5 \times 10^6 \, M_\odot$. The projected half-mass radius of these clusters is significantly larger than 1 pc, the value we have adopted for our reference model. Those large radii may mislead one to expect much larger relaxation times and, consequently, little or no evolution of the η over time. However, we note that Mengel et al. (2002) fitted King models with a concentration parameter $\Psi/\sigma \approx 6$ to the light profiles of their clusters. Such King models are significantly more concentrated than the Plummer model that we used in the calculations performed here. In fact, it turns out that a King model with $\Psi/\sigma = 6$, a half-mass radius of 2–3 pc (cf. table 3 of Mengel et al. 2002) and a mass of some 500 000 $M_\odot$, has a mean density within its core radius that essentially equals the mean density within the half-mass radius of our reference Plummer model. Consequently, the rapid evolution of η found in this article should be applicable to the dynamics in the core of some Antennae clusters, implying that the core regions of very rich clusters are still affected by strong segregation despite their very low age, a conclusion also reached by de Grijs, Wilkinson & Tadhunter (2005) using observational arguments. As a result, the core will appear more compact, while the half-mass radius is left largely unchanged, a situation that leads to King model fits with higher values of Ψ/σ than is appropriate (cf. also Boily et al. 2005, for examples of this effect).

8 DISCUSSION

This paper investigated possible biases when estimating the dynamical mass of young and dense stellar systems from spectrophotometric data. Using the virial theorem, one may convert observed half-*light* radius and flux-weighted mean velocity dispersion to mass through the dimensionless parameter η defined in equation (3). This factor will vary with time due to mass segregation whenever the two-body relaxation time in equation (8) is short: the heavy bright stars segregate to the centre rapidly. A parameter space exploration led us to conclude that for clusters where $t_{r0} \lesssim 200$ Myr η may increase by a factor of 2 compared with its initial value, whereas if $t_{r0} \gtrsim 500$ Myr then very little evolution of η will take place within the first 100 Myr. Meanwhile, the mass distribution and potential, dominated by fainter stars, remains largely unchanged, so that light does not follow mass anymore.

We can synthesize the main features of this bias in η in a diagram of cluster age versus relaxation time derived from observations. Substituting the projected half-mass radius R_{hm} and the total mass M for r_g and N in equation (8), we get

$$t_{r0} = \frac{2 \times 0.138 \, \eta_0^{1/2}}{G \, \langle m \rangle \, \sqrt{3} \, \ln \Lambda} \, R_{hm}^2 \, \sigma_{m1d}, \tag{33}$$

where $\langle m \rangle$ is given by the IMF and $\ln \Lambda$ is the Coulomb logarithm [for which we adopted $\ln (0.4N)$ previously]. The same formula applied to *observed* quantities would give an estimated relaxation time

$$t_{r,obs} = \frac{2 \times 0.138 \, \eta_0^{1/2}}{G \, \langle m \rangle \, \sqrt{3} \, \ln \Lambda} \, R_{hl}^2 \, \sigma_{los}. \tag{34}$$

With the ratio η/η_0 given by equation (7) we obtain a ratio of 'true' to measured relaxation times,

$$\frac{t_{r0}}{t_{r,obs}} = \left(\frac{\eta}{\eta_0} \right)^2 \left(\frac{\sigma_{los}}{\sigma_{m1d}} \right)^3. \tag{35}$$

The ratio of squared velocity dispersion was found not to decrease by more than 10 per cent throughout the simulation time; we may therefore set $\sigma_{los}/\sigma_{m1d} = 1$ in equation (35). Equation (35) together with equation (31) can be solved with input cluster age and measured relaxation time to obtain a unique pair (t_{r0}, η). It is then straightforward to draw lines of constant η in a graph of age versus $t_{r,obs}$ axes and recover the true relaxation time of the mass profile (since we must have $t_{r0} = t_{r,obs}$ at time $t = 0$ by construction and the potential does not change).

Fig. 16 graphs the contours lines of constant η/η_0 in the plane $t_{r,obs}$–age. All clusters start off on the age = 0 axis which coincides with the contour $\eta/\eta_0 = 1$. As the cluster becomes older and mass segregation sets in, the time evolution marks a path that is seen to drift to shorter (measured) relaxation times and larger η. Each level is indicated on the graph. The path for our reference model is shown along with a second model of initial half-mass relaxation time of 400 Myr. Note that even for this model $t_{r,obs}$ drops to ≈ 200 Myr

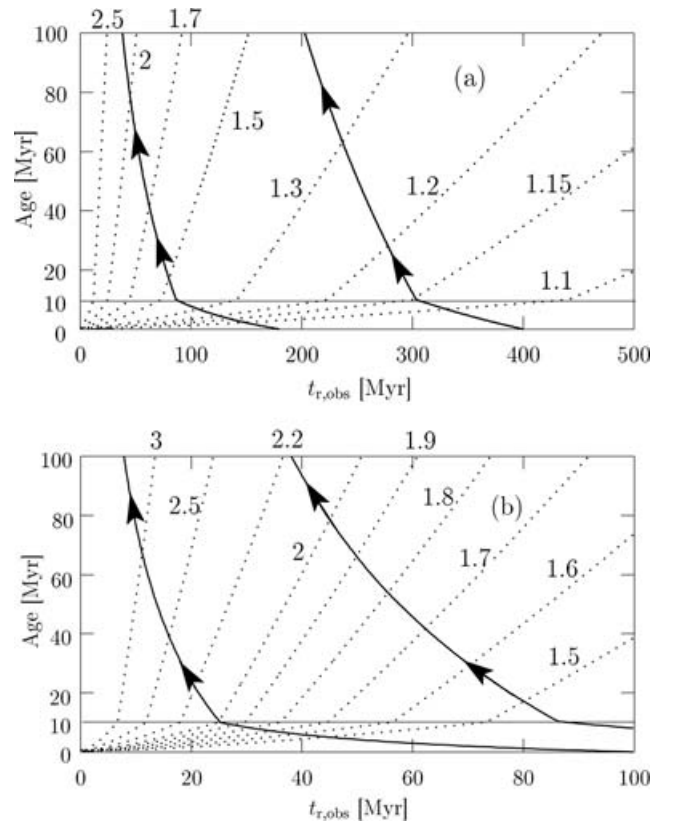**Figure 16.** Contours of constant $\eta(t)/\eta_0$ (dotted curves) in the plane of cluster age versus relaxation time, $t_{r,obs}$, derived from cluster observables. The contours were constructed using the bilinear interpolation scheme of Section 7.1. The contour $\eta(0)/\eta_0 = 1$ coincides with the horizontal axis (cluster age = 0). (a) The solid lines trace the evolution in time of η/η_0 for two model clusters with initially $t_{r,obs} = 180$ and 400 Myr. The arrows point to the future. The value of $t_{r,obs}$ decreases with age, always, while $\eta(t)/\eta_0$ increases. (b) Same as (a) but now one of the models has $t_{r,obs} = 100$ Myr initially. The evolution track for that case crosses contours of yet higher values of $\eta(t)/\eta_0$ at fixed age. Note the change of scale on the abscissa.

after 100 Myr of evolution: at that time its mass is underestimated by ≈30 per cent. Fig. 16(b) zooms in on the interval [0:100] Myr of the $t_{\rm r,obs}$-axis.

As seen in Fig. 16, the most dramatic evolution in η occurs in the first 10 Myr. Furthermore, if only the most luminous stars were used as tracers, still higher factors η/η_0 would be expected (cf. Fig. 6). For the young massive Antennae clusters for which the measured relaxation time $t_{\rm r,obs} > 500$ Myr, mass segregation is negligible when applied to these clusters as a whole. We noted, however, that our reference model provides a good fit to the core region of some of these clusters in terms of mass and density. Thus, mass segregation may yet prove an efficient agent for evolution in the central part of massive young clusters, a process that would contribute to make the core look more compact than it really is and so inflate the concentration parameter $c = \log(r_{\rm h}/r_{\rm c})$ of King model fits to these clusters. Examples of this phenomenon are given in Boily et al. (2005).

Light curves have been used to estimate colour indices averaged over two surface elements bounded by the projected half-light radius. The difference between these colour indices taken as a function of time shows that the inner part becomes bluer by 0.05 dex so long as massive stars have not reached the red giant state. At that time and for all times thereafter, the inner region becomes redder (by more than 0.05 dex). Colours should be interpreted with caution. The evolution of $V - K$ is highly sensitive to the properties of the red stages of stellar evolution, and especially to the red supergiant and AGBs. Such fine details of stellar evolution, often model dependent and difficult to pin down with precision, have less bearing on the colour *gradients* because these giants stars dominate the light in the red wherever they are, and hence Δ_{V-K} quantifies their concentration in space. The stellar evolution tracks used here tend to exaggerate the role of bright red stars. Discarding the most luminous red supergiants or TP-AGB stars altogether reduces the gradients by a few hundredths of a magnitude at most.

The evolution of the stellar mass function within the model clusters was also quantified through variations in the power indices defined for the IMF equation (18). We noted that the variations of the power index β during evolution are a good match to those observed in the LMC cluster NGC 1818 (Gouliermis et al. 2004). However, the initial relaxation time of the more concentrated model used in this section of ∼115 Myr is significantly smaller than the one derived for this cluster [we compute ∼250 Myr from equation (8); see also Elson et al. 1987] which implies that dynamical mass segregation alone does not account for gradients in the stellar population for the cluster as a whole. Thus, we would argue that a fair degree of primordial stellar segregation must be relied on to explain that cluster photometry. Despite this caveat, it is well worth repeating that the *central* relaxation time of NGC 1818 of some 120 Myr is of order of the half-mass relaxation time of the model used, and therefore dynamical segregation surely has played a role in the evolution of the stellar mass function near the centre (see also de Grijs et al. 2002b). Our view is that a set of models tailored to that particular cluster will be required to disentangle fully primordial from evolutionary effects.

With $\eta(t_{\rm r0}, t)$ derived from equation (31), it was possible to construct a log-Gaussian cluster mass function and carry out a statistical survey of the impact of mass segregation on the shape of the observed CMF obtained from assuming no evolution of η, to the CMF derived from taking into account the time-evolution of η (Fig. 16). The actual total integrated mass of the CMF is 50 per cent larger than the apparent one for the case describe in Fig. 15(a) and

20 per cent for Fig. 15(b). This has direct bearing on the global SFR derived for galaxy mergers and starburst galaxies in general. We noted that the two CMFs so constructed differ mostly at the low-mass range ($<500\,000\,{\rm M_\odot}$) where the relaxation time is significantly shorter. To quantify this effect, we found a shift in the peak of the real CMF towards high masses compared to the 'observed' CMF. This shift is on the order of 0.2 dex for a distribution of relaxation times centred around 200 Myr and is lower when this mean relaxation time is larger (Table 3). Furthermore, we also found a slight widening of the observed CMF, by a logarithmic factor of ≃0.05 (see Fig. 15). This would have some influence on evolutionary predictions of cluster mass functions. Vesperini (1998) has shown that the Milky Way CMF may well shift to *smaller* masses by ≃0.1 dex over a Hubble time due to tidal destruction and other effects. The trend we found here goes in the opposite direction, however it is only operative for clusters with short relaxation times. As clusters are possibly more massive than estimated from observations but also less concentrated (lower King fitting parameter) it is not clear how tides and other disruptive effects will shape up the CMF, especially if the host galaxy itself is out of equilibrium. A set of fully three-dimensional N-body simulations could enhance our knowledge of the influence of mass segregation on longer time-scales and with strong tidal fields found, for example, in merging galaxies.

Our models of isolated clusters suffer a few important limitations. We have mentioned the role that tidal fields will play in removing weakly bound stars. Another aspect of the problem is the possibly low star formation efficiency when the cluster forms. We mentioned how gas from stellar winds might impact on the dynamics (Section 6.3). Residual gas from the formation epoch will also drive much evolution in the early stages by bringing the cluster out of virial equilibrium (Elson et al. 1989; Kroupa & Boily 2002, see also Bastian & Goodwin 2006). Yet another aspect is our tacit assumption that stars are all born at the same time and all evolve in unison. Stars in massive clusters may well have ages that vary by a few Myr. This will have some bearing on the rise of η in the early stages because not all the stars become remnant at the same time, leading to enhanced mass segregation and further increase in η. For instance, the knee seen at $t \approx 10$ Myr may well increase to yet higher values before shifting over to the slower rate of increase that we have advertized (Fig. 6).

A more severe limitation however, one that will impact on η at all times, is the fraction of primordial binaries. Tight binaries will survive for eons and in particular a very large fraction of them will survive for the short times that are of interest here. The presence of binaries and multiple stars naturally enhances the observed velocity dispersion which biases the mass estimate to larger values through the virial theorem. However, binaries also instantly broaden the width of the effective stellar IMF, since, roughly speaking, they will dynamically act as single stars of mass equal to the sum of their member stars. If the fraction of primordial binaries is low, the mean stellar mass will remain unchanged but the maximum mass will effectively double. The net effect, then, is similar to halving the mass-segregation time-scale $t_{\rm ms}$ by reducing the mean stellar mass. This can be accomplished by increasing the power index α of the IMF in equation (18). We have found after ≈10 Myr of evolution for the extreme case where $\alpha = 2.3$ (Salpeter value) that η has nearly increased by 30–50 per cent in comparison with the result for the standard case $\alpha = 1.3$. These considerations clearly point to yet more rapid evolution and the need for more realistic models than is affordable here to pin down more precisely the dynamics of young massive clusters.

REFERENCES

Anders P., Fritze-v. Alvensleben U., 2003, A&A, 401, 1063
Bastian N., Goodwin S. P., 2006, MNRAS, in press (doi: 10.1111/j.1745-3933.2006.00162.x)
Bessell M. S., 1990, PASP, 102, 1181
Bessell M. S., Brett J. M., 1988, PASP, 100, 1134
Bettwieser E., Inagaki S., 1985, MNRAS, 213, 473
Boily C. M., Lançon A., Deiters S., Heggie D. C., 2005, ApJ, 620, L27
Bressan A., Fagotto F., Bertelli G., Chiosi C., 1993, A&AS, 100, 647
Bruzual G., Charlot S., 2003, MNRAS, 344, 1000
Charlot S., Bruzual A. G., 1991, ApJ, 367, 126
de Grijs R., Johnson R. A., Gilmore G. F., Frayn C. M., 2002a, MNRAS, 331, 228
de Grijs R., Gilmore G. F., Johnson R. A., Mackey A. D., 2002b, MNRAS, 331, 245
de Grijs R., Wilkinson M. I., Tadhunter C. N., 2005, MNRAS, 361, 311
Deiters S., 2001, PhD thesis Univ. Heidelberg (http://www.ub.uni-heidelberg.de/archiv/1831)
Elson R. A. W., 1991, ApJS, 76, 185
Elson R. A. W., Fall S. M., Freeman K. C., 1987, ApJ, 323, 54
Elson R. A. W., Freeman K. C., Lauer T. R., 1989, ApJ, 347, L69
Farouki R. T., Salpeter E. E., 1982, ApJ, 253, 512
Figer D. F., 2005, Nat, 434, 192
Giersz M., Heggie D. C., 1994, MNRAS, 268, 257
Giersz M., Spurzem R., 1994, MNRAS, 269, 241
Girardi L., Bertelli G., 1998, MNRAS, 300, 533
Gouliermis D., Keller S. C., Kontizas M., Kontizas E., Bellas-Velidis I., 2004, A&A, 416, 137
Gürkan M. A., Freitag M., Rasio F. A., 2004, ApJ, 604, 632
Heggie D. C., Mathieu R. D., 1986, Lecture Notes in Physics, 267, 233
Hunter D. A., Light R. M., Holtzman J. A., Lynds R., O'Neil E. J., Grillmair C. J., 1997, ApJ, 478, 124
Hurley J. R., Pols O. R., Tout C. A., 2000, MNRAS, 315, 543
Khalisi E., Amaro-Seoane P., Spurzem R., 2006, MNRAS, submitted (astro-ph/0602570)
Kroupa P., 2002, Sci, 295, 82
Kroupa P., Boily C. M., 2002, MNRAS, 336, 1188
Lamers H. J. G. L. M., Anders P., de Grijs R., 2006, A&A, in press (astro-ph/0601606)
Larson R. B., 1970, MNRAS, 147, 323
Lejeune T., Cuisinier F., Buser R., 1997, A&AS, 125, 229
Lejeune T., Cuisinier F., Buser R., 1998, A&AS, 130, 65
Louis P. D., Spurzem R., 1991, MNRAS, 251, 408
Lynden-Bell D., Eggleton P. P., 1980, MNRAS, 191, 483
Lynden-Bell D., Wood R., 1968, MNRAS, 138, 495
McCrady N., Gilbert A. M., Graham J. R., 2003, ApJ, 596, 240
McCrady N., Graham J. R., Vacca W. D., 2005, ApJ, 621, 278
Mengel S., Lehnert M. D., Thatte N., Genzel R., 2002, A&A, 383, 137
Meylan G., Heggie D. C., 1997, A&AR, 8, 1
Mouhcine M., Lançon A., 2003, A&A, 402, 425
Pols O. R., Schroder K., Hurley J. R., Tout C. A., Eggleton P. P., 1998, MNRAS, 298, 525
Portegies Zwart S. F., McMillan S. L. W., 2002, ApJ, 576, 899
Schaller G., Schaerer D., Meynet G., Maeder A., 1992, A&AS, 96, 269
Smith L. J., Gallagher J. S., 2001, MNRAS, 326, 1027
Spitzer L. J., 1969, ApJ, 158, L139
Spitzer L., 1987, Dynamical Evolution of Globular Clusters. Princeton Univ. Press, Princeton, NJ, p. 191
Spitzer L., Shull J. M., 1975, ApJ, 201, 773
Spurzem R., 1992, Rev. Mod. Astron., 5, 161
Spurzem R., Takahashi K., 1995, MNRAS, 272, 772
Vesperini E., 1998, MNRAS, 299, 1019

This paper has been typeset from a TEX/LATEX file prepared by the author.